Article:

Liu, Y. orcid.org/0000-0002-3065-9872, Ye, J. orcid.org/0000-0002-6857-7450, Yang, Y. et al. (4 more authors) (2023) Experimental study on wire and arc additively manufactured steel double-shear bolted connections. Journal of Building Engineering, 76. 107330. ISSN 2352-7102

https://doi.org/10.1016/j.jobe.2023.107330

Experimental study on wire and arc additively manufactured steel double-shear bolted connections

Yunyi Liu[1,2], Jun Ye[4,*], Yuanzhang Yang[1], Guan Quan[1], Zhen Wang[3], Weijian Zhao[1,2], Yang Zhao[1]

1. College of Civil Engineering and Architecture, Zhejiang University, Hangzhou, 310058, China
2. Center for Balance Architecture, Zhejiang University, Hang Zhou, 310014, China
3. Department of Civil Engineering, Zhejiang University City College, Hangzhou, 310015, China
4. School of Civil Engineering, University of Leeds, Leeds, LS2 9JT, UK

Abstract

Wire and arc additive manufacturing (WAAM) has emerged as a highly promising technique for manufacturing large-scale steel structural elements. However, the distinct mechanical properties of WAAM steel could potentially lead to different performance of WAAM steel bolted connections compared to the traditional steel bolted connections. This study aims to investigate the material properties of WAAM steel and the structural behaviours of WAAM steel bolted connections, focusing on the effects of print layer orientation and connection plate geometrical dimensions. A total number of 24 WAAM steel coupon specimens with three different print layer orientations and 36 WAAM double-shear bolted connections with two print layer orientations and different geometric dimensions were designed, fabricated and tested under monotonic tension. These specimens were measured using a 3D laser scanner and Digital Image Correlation (DIC) was adopted to measure the structural response during testing. The impact of print layer orientations on WAAM material properties and the effects of WAAM material properties on bolted connections were analysed and discussed. The current design codes for traditional steel bolted connections were evaluated against the test results of WAAM steel bolted connections. The study found that the print layer orientations of WAAM steel plates initiated an anisotropic material property of the coupon specimens, demonstrated by the differences in ultimate tensile strength and strain of specimens with different print layer orientations. Five failure modes, including net section tension, shear-out, bearing, end-splitting, and block shear failure were observed for the bolted connections. The material anisotropy further affects the performance of the bolted connections, though in the same dimensions, 28% of the specimens presented different failure modes due to the different print layer orientations. The effectiveness of current steel design standards was compromised by inaccurate predictions of failure modes due to the distinct end-splitting failure mode and the effects of material anisotropy, though the predictions of the ultimate capacities of the WAAM lap shear specimens were relatively accurate.

Keywords: 3D printing; Wire arc additive manufacturing; Double-shear bolted connections; Failure modes; Design approaches

1. Introduction

Additive manufacturing (AM) has prevailed in aerospace, automotive, and other highly automated production domains, and recently it has been prospering in civil engineering, targeting on concrete and metal materials [1-5]. Wire and arc additive manufacturing (WAAM), as one means of the Directed Energy Deposition (DED) technologies, has shown significant potential in the construction industry for its ability to fabricate large-scale and complex steel structural elements. It has the advantages of fast production speed, low equipment cost, high material utilization, and high sustainability compared to conventional manufacturing methods [6-11].

The basic material properties and structural performance of WAAM components are worthy of research to fully exploit the potential of WAAM technology in the construction sector. Specifically, regarding the WAAM steel, various experimental studies have been conducted focusing on the mechanical properties and microstructures [12-26]. According to the current literature, the WAAM-manufactured steel exhibits a non-negligible level of anisotropy corresponding to the print layer orientation of the test specimens due to the distinct approach of steel additive manufacturing [19, 20]. However, the WAAM carbon steel specimens extracted from various orientations and locations could show an overall isotropic mechanical behaviour after being machined. Further research is still required to clarify the anisotropic behaviour of WAAM steel, considering the existing printing approaches, printing parameters and processing methods [26].

Regarding the WAAM components, the tubular beams [27] and columns [28-30] with various cross-sectional shapes have been tested to analyse the material properties and geometric dimensions of WAAM steel on the structural performance. The studies reveal that the geometric variability of WAAM steel elements is higher compared to conventionally formed steel elements, highlighted by a weakening effect on ultimate capacities [28]. WAAM technology has also been applied in a full-scale structure, with the world's first metal 3D-printed bridge being manufactured [3]. Simulations and tests have demonstrated that the 3D printed bridge was able to carry the full design load [3].

Due to the manufacturing (e.g., overhang problem) and dimensional constraints of 3D printing technology, the target structures may need to be printed in parts and assembled by connections afterwards [4]. In traditional steel structures, welding and bolt connection are the most widely used approaches for assembling. Welding can be a good means of assembling but residual stress could be further produced which can affect the structural performance of 3D-printed steel [31]. Bolted connections can be an alternative for the future application of 3D-printed steel structures due to the ease of on-site operation.

Previous studies have extensively investigated the failure modes and ultimate capacities of conventionally manufactured steel bolted connections [32-39]. Winter [38] defined four different failure modes for bolted connections, including net section tension, shear-out, bearing and bolt shearing failures. The ultimate capacities corresponding to these failure modes have been fully studied [40-44] and included in design codes including AS/NZS 4600 [45], AS 4100 [46], AISI S100 [47], AISC 360 [48], EN 1993-1-1 [49], EN 1993-1-3 [50], and EN 1993-1-8

[51]. Additional failure modes, including end-splitting and tilt-bearing failure, were also explored and the corresponding design approaches were furtherly developed by various researchers [52-54].

As the effects of WAAM steel properties and printing strategies on the performance of bolted connections are not fully clear, the existing design provisions for traditional steel structures may not be appropriate to the design of WAAM steel bolted connections. The current research focusing on the structural performance of bolted connections of WAAM steel is still limited. Guo et al. [55, 56] tested the structural behaviour of WAAM steel bolted connections with different geometric parameters. It was concluded that the print layer orientation had no significant influence on the structural performance, shown by a 5% average difference between the ultimate capacities of specimens with different print layer orientations. However, a few specimens exhibited a significantly larger discrepancy (15%), which indicates that further investigations are still required to explore the impacts of material anisotropy on the WAAM bolted connections. The existing design approaches should also be evaluated to show whether the distinct material properties of WAAM steel should be considered in the predictions of the performance of the bolted connections.

This paper presents an experimental investigation into the mechanical properties of WAAM steel plates and double-shear WAAM steel bolted connections under monotonic loadings. Considering the print layer orientations and geometrical dimensions, 24 identically-sized tensile coupons and 36 double-shear connection specimens were designed, fabricated and tested. These specimens were measured using a 3D laser scanner and Digital Image Correlation (DIC) was adopted to measure the structural responses during testing. Analyses and discussions on the impact of print layer orientations on WAAM material properties and the impact of WAAM material properties on the ultimate capacities of bolted connections were conducted. The current design codes for traditional steel structures were evaluated against the test results. This research provides a comprehensive understanding of material properties and structural performances of WAAM bolted connections, thereby facilitating future utilization of 3D printing technology in the construction industry.

2. Existing design equations for bolted connections

As there was no design provision for 3D-printed bolted connections, this section presented the strength design equations for a single-bolt double-shear connection with different geometries, available in the existing design codes of traditional steel structures and recent literature. The reviewed equations could be potentially used as the foundation and furtherly developed for the prediction of ultimate capacities of 3D-printed steel structures. Four failure modes (bolt shearing, net section tension, shear-out, and bearing failure) have been included in these equations, as shown in Figure 1.

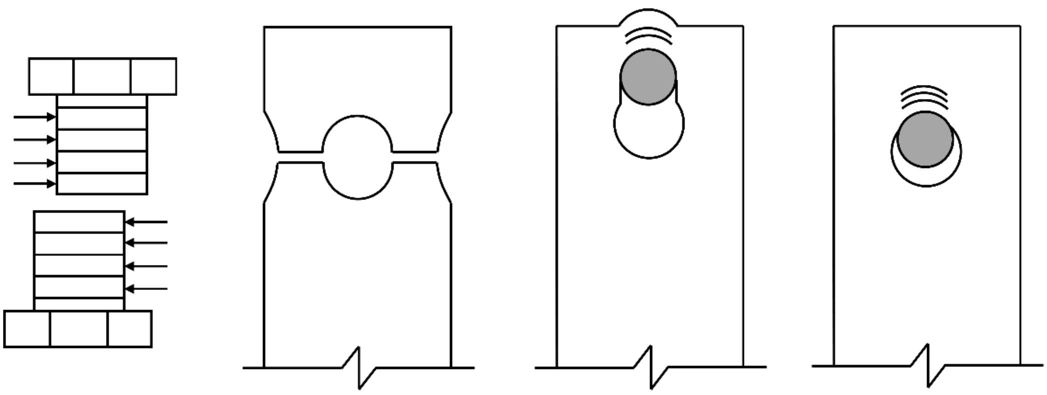

(a) (b) (c) (d)

Figure 1. Schematic representation of failure modes: (a) bolt shearing, (b) net section tension, (c) shear-out, and (d) bearing failure

The general equations for net section tension (NS), shear-out (SO), and bearing failure (B) could be summarized as Eq. (1), Eq. (2), and Eq. (3), respectively.

$$P_{\mathrm{ns}} = C_{\mathrm{ns}} A_{\mathrm{n}} f_{\mathrm{u}} \tag{1}$$

$$P_{\mathrm{so}} = C_{\mathrm{so}} L_{\mathrm{so}} t f_{\mathrm{u}} \tag{2}$$

$$P_{\mathrm{b}} = C_{\mathrm{b}} d_{\mathrm{f}} t f_{\mathrm{u}} \tag{3}$$

where, P is the predicted capacities for corresponding failure type, C is the coefficient corresponding to the related failure mode, A_{n} is the net sectional area for NS failure, L_{so} is the shear plane length for SO failure, t is the thickness of the plate, d_{f} is the nominal bolt diameter, and f_{u} is the tensile strength of steel.

However, for each failure mode, the value of coefficients developed were generally different, as summarised in Table 1. For the net section tension failure, C_{ns} was developed to account for the non-uniform distribution of tensile stresses across the net section failure. AS/NZS 4600 [45] and AISI S100 [47] set C_{ns} as $0.9 + (0.1d_{\mathrm{f}}/b)$, whilst for EN 1993-1-3 [50], it was $1 + 3(d/b - 0.3)$. AS 4100 [46] adopted a constant of 0.85. EN 1993-1-1 [49] specified $k = 1$ for smooth holes made by drilling or water jet cutting and $k = 1$ for rough holes made by punching or flame cutting. AISC 360 [48] did not use any coefficient for net section failure.

Table 1. Summary of design equations

Specifications	Failure modes		
	Net section	Shear-out	Bearing
AS/NZS 4600:2018 [45]	$P_{\mathrm{ns,NZS}} = \left[0.9 + \left(\frac{0.1d_{\mathrm{f}}}{b}\right)\right] A_{\mathrm{n}} \mathrm{f}_{\mathrm{u}}$	$P_{\mathrm{so,NZS}} = e_1 t f_{\mathrm{u}}$	$P_{\mathrm{b,NZS}} = \alpha C d_{\mathrm{f}} t f_{\mathrm{u}}$

AS 4100:2020 [46]	$P_{\mathrm{ns,AS}} = 0.85A_{\mathrm{n}}f_{\mathrm{u}}$	$P_{\mathrm{so,AS}} = (e_1 - \frac{d}{2})tf_{\mathrm{u}}$	$P_{\mathrm{b,AS}} = 3.2d_{\mathrm{f}}tf_{\mathrm{u}}$
AISI S100:2016 [47]	$P_{\mathrm{ns,NZS}} = \left[0.9 + \left(\frac{0.1d_{\mathrm{f}}}{b}\right)\right]A_{\mathrm{n}}\mathrm{f_u}$	$P_{\mathrm{so,AISI}} = 1.2(e_1 - \frac{d}{2})tf_{\mathrm{u}}$	$P_{\mathrm{b,NZS}} = \alpha Cd_{\mathrm{f}}tf_{\mathrm{u}}$
AISC 360:2022 [48]	$P_{\mathrm{ns,AISC}} = A_{\mathrm{n}}f_{\mathrm{u}}$	$P_{\mathrm{so,AISC}} = 1.5(e_1 - \frac{d}{2})tf_{\mathrm{u}}$	$P_{\mathrm{b,AISC}} = 3d_{\mathrm{f}}tf_{\mathrm{u}}$
EN 1993-1-1:2020 [49]	$P_{\mathrm{ns,EN1}} = kA_{\mathrm{n}}f_{\mathrm{u}}$	-	
EN 1993-1-8:2021 [51]	-	$P_{b,EN8} = \alpha_{\mathrm{t}}k_{\mathrm{m}}d_{\mathrm{f}}tf_{\mathrm{u}}$	
EN 1993-1-3:2022 [50]	$P_{\mathrm{ns,EN3}} = \left(1 + 3\left(\frac{d}{b} - 0.3\right)\right)A_{\mathrm{n}}f_{\mathrm{u}}$	$P_{\mathrm{b,EN3}} = 2.5\alpha_{\mathrm{b}}k_{\mathrm{t}}d_{\mathrm{f}}tf_{\mathrm{u}}$	

Note: e_1 is the end distance, d is the diameter of the bolt hole, b is the plate width, α is 1.33 for the double shear connection without washers. When $d_{\mathrm{f}}/t < 10$, the bearing factor $C = 3.0$, when $10 < d_{\mathrm{f}}/t < 22$, $C = 4 - 0.1(d_{\mathrm{f}}/t)$, and when $d_{\mathrm{f}}/t > 22$, $C = 1.8$. α_{b} is the minimum value of 1 and $e_1/3d_{\mathrm{f}}$. When $0.75\mathrm{mm} < t < 1.25mm$, $k_{\mathrm{t}} = (0.8t + 1.5)/2.5$, and when $t > 1.25mm$, $k_{\mathrm{t}} = 1$. α_{t} is the minimum of e_1/d, $3f_{\mathrm{ub}}/f_{\mathrm{u}}$, and 3, For steel grades equal to or higher than S460, $k_{\mathrm{m}} = 0.9$; otherwise $k_{\mathrm{m}} = 1$.

Similarly, for shear-out failure, different design codes employed different shear planes length L_{so} and shear coefficients C_{so}. AS/NZS 4600 [45] utilized e_1 as the shear plane length, whereas AS 4100 [46], AISI S100 [47], and AISC 360 [48] employed $e_1 - d/2$ as the shear plane length. The corresponding shear coefficients for the four codes were 0.5, 0.5, 0.6, and 0.75 respectively. EN 1993-1-3 [50] and EN 1993-1-8 [51] stipulated that the shear-out and bearing failure as one type of failure mode but took different values of coefficient C_{b}.

For bearing failure, the coefficient C_{b} was usually related to three geometric parameters: t, e_1, and d_{f}. AS/NZS 4600 [45] and AISI S100 [47] set C_{ns} as αC. C varied with the ratio of bolt diameter and plate thickness d_{f}/t. EN 1993-1-8 [51] set C_{ns} as $\alpha_{\mathrm{t}}k_{\mathrm{m}}$, and EN 1993-1-3 [50] set C_{ns} as $2.5\alpha_{\mathrm{b}}k_{\mathrm{t}}$, as shown in Table 1. AS 4100 [46] and AISC 360 [48] adopted values of 3.2 and 3, respectively.

Teh and Uz [43] proposed Eq. (4) by introducing an active shear length $L_{av} = e_1 - d/4$, and a modification of Eq. (5) was recommended considering the catenary action [44]. Lyu et al. [54] employed a new Eq. (6) to estimate the ultimate bearing capacity, which considered the potential occurrence of splitting failure. The reduction factor φ varied with the value of e_1/d, however, the relationships between the two displayed a different trend. Lyu et al. [54] recommended a reduction factor of $\varphi = 0.9$. A design equation for bearing failure had been proposed, incorporating a different coefficient of 3.5 [34]:

$$P_{\mathrm{so,1}} = 1.2(e_1 - \frac{d}{4})tf_{\mathrm{u}} \tag{4}$$

$$P_{\mathrm{so,2}} = 1.2(\frac{3d_{\mathrm{f}}}{e_1})^p(e_1 - \frac{d}{4})tf_{\mathrm{u}} \tag{5}$$

$$P_{\mathrm{so,3}} = \begin{cases} 1.04\frac{e_1}{d}d_{\mathrm{f}}tf_{\mathrm{u}}, e_1/e_2 \leq 0.5 \\ \varphi P_{\mathrm{so,3}}, e_1/e_2 > 0.5 \end{cases} \tag{6}$$

$$P_{\mathrm{b}} = 3.5d_{\mathrm{f}}tf_{\mathrm{u}} \tag{7}$$

where, p is the influence degree of catenary action, taken as 1/10 herein for the WAAM connections.

3. Experimental programme

3.1 Materials and specimens

The test specimens were extracted from the flat surfaces of oval tubes produced utilizing the WAAM technology following the printing parameters presented in Table 2. The used feedstock was welding wire ER50-6, with the chemical compositions and mechanical properties listed in Table 3 and Table 4, respectively.

Table 2. Printing parameters of specimens with a nominal thickness of 3mm

Travel speed (m/min)	Wire feed rate (m/min)	Wire diameter (mm)	Welding voltage (V)	Layer thickness (mm)	Bead width (mm)	Temperature (°C)	Humidity (%RH)	Shielding gas
0.65-0.7	4.0	1.2	19.5	1.8	5	12-21	35-55	97%Ar+ 3%CO_2

Table 3. Chemical compositions (% by weight) of ER50-6 low carbon steel feedstock

Chemical compositions	C	Mn	Si	P	S	Cr	Ni	Cu	Mo	V
ER50-6	0.074	1.47	0.85	0.015	0.01	0.023	0.009	0.1	0.004	0.002

Table 4. Mechanical properties of ER50-6 low carbon steel feedstock

	Tensile Strength (MPa)	Yield Strength (MPa)	Elongation Rate (%)	Charpy V Impact Test Value at 40°C (J)
ER50-6	554	445	26	96

To investigate the influence of print layer orientations on the mechanical properties of WAAM steel, a total of 24 tensile coupons with θ angles of 0°, 45°, and 90° (see Figure 2(a)) were designed. All the coupon specimens had a nominal cross-section of 37.5 mm^2 with a nominal thickness of 3mm.

Whilst, a total of 36 lap shear test specimens with varying geometric parameters (see Figure 2(b)) and print layer orientations were designed and fabricated to show their impacts on the structural performance of WAAM bolted connections. For each set of geometric parameters, two specimens with different angles θ between the specimen and the print layer orientations of 0° and 90° were manufactured, as shown in Figure 2(a).

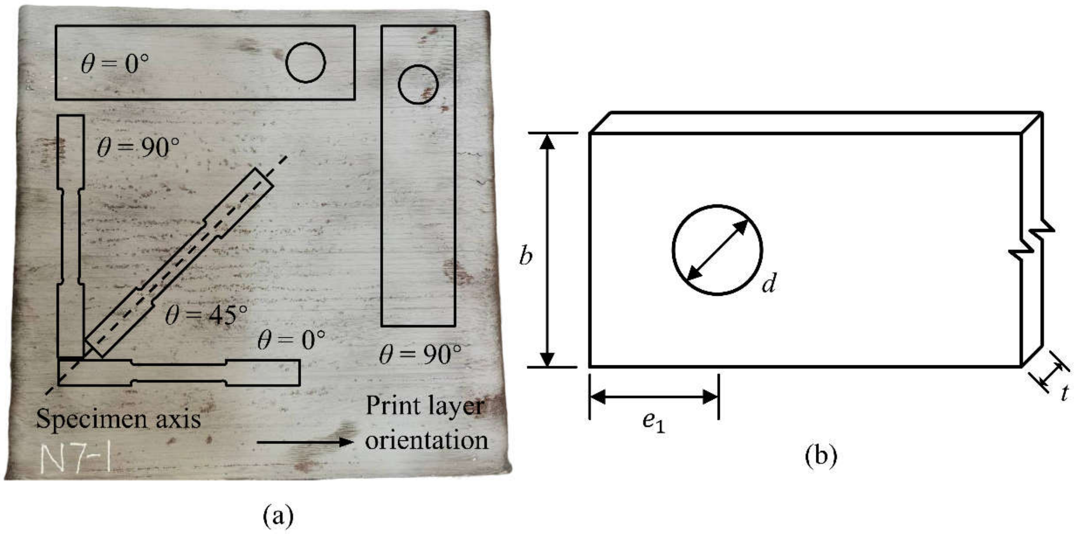

Figure 2. (a) Specimens extracted from flat plates at different orientations and (b) basic configuration of test specimens

Each WAAM connected plate was labelled as $\mathrm{HD3} - d - b - e_1$ or $\mathrm{VD3} - d - b - e_1$ (d, b and e_1 were introduced before). The letter 'H' or 'V' indicated that the plate was extracted horizontally or vertically to the print layer orientation, with the relative angle θ being 0° or 90°, respectively. The letter 'D' represented the double-shear connection type, followed by the nominal thickness t of 3 mm.

High-strength steel plates were used in the bolted connections to ensure the failure occurring within the WAAM steel plates, which had 4 mm thickness with a measured yield strength $f_{\mathrm{y,HSS}}$= 819 MPa and a measured tensile strength $f_{\mathrm{u,HSS}}$= 886 MPa. The grade 12.9 high-strength bolts and nuts were selected, to prevent bolt shearing. The high-strength steel plates were named following the same form as WAAM steel plates, such as HSS4-18-30-27, where "HSS" indicated high-strength steel.

3.2 Geometric measurements

3.2.1 Measurement method

Due to the undulating surfaces of the WAAM steel plates, traditional measurement methods could not fully capture the geometric dimensions of the specimens. Therefore, a 3D laser scanner was used to measure the geometric dimensions of the test specimens, which had a maximum scanning rate of 2020000/s, an accuracy of 0.02 mm and a maximum resolution of 0.025 mm. The average error of the scanning data was within 2%, when applied to WAAM test steel plates. The scan data of the steel plates was recorded as point clouds, and post-processed by eliminating grid errors and repairing imperfections. After obtaining the post-processed models, the actual geometric parameters of the specimens were calculated, following the process, shown in Figure 3 and described by Kyvelou et al. [19].

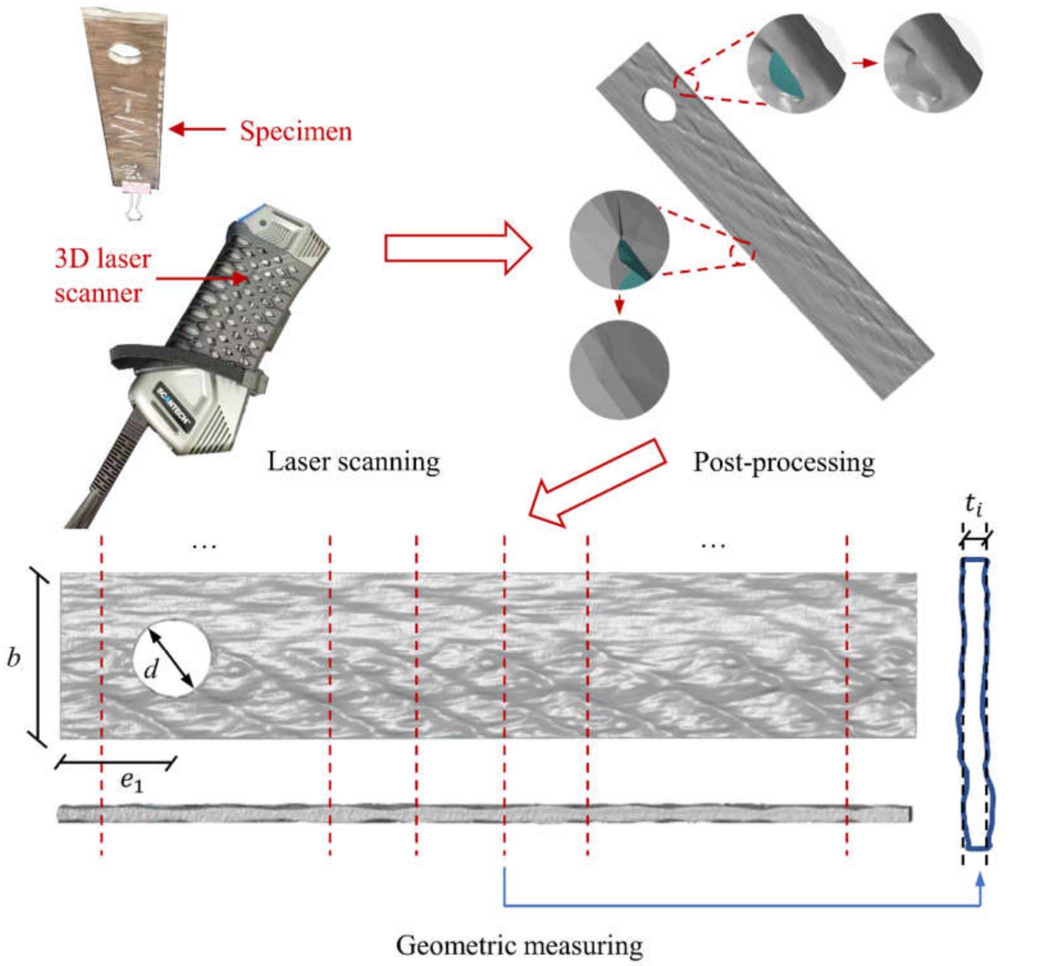

Figure 3. Scanning and measuring process

3.2.2 Measurement results

The thickness and cross-sectional area were calculated at a contour spacing of 0.1 mm along the longitudinal direction of the gauge length of the coupon specimens, as shown in Table 5. The minimum A_{std} and t_{std} values were observed in coupons with a θ of 0° among the three print layer orientation coupons, indicating the least variation in cross-sectional area and thickness. This could be attributed to the similarity of all cross-sections perpendicular to the direction of deposition paths. In contrast, greater variation in cross-sections was observed for coupons with θ of 45° and 90°. The coupon thickness t varied from 2.6 mm to 4.1 mm, 2.4 mm to 5.1 mm, and 2.6 mm to 4.8 mm for coupons with θ of 0°, 45° and 90°, respectively. Whilst the coupon cross-sectional area A varied from 40.8 mm^2 to 44.2 mm^2, 39.7 mm^2 to 52.3 mm^2, and 36.7 mm^2 to 50.7 mm^2, respectively.

Table 5. Variation of the thickness of coupon specimens

t_{nom} (mm)	θ (°)	A_{mean} (mm^2)	A_{max} (mm^2)	A_{min} (mm^2)	A_{std} (mm^2)	t_{mean} (mm)	t_{max} $(mm^2$	t_{min} $(mm^2$	t_{std} (mm)
	0	42.3	44.2	40.8	0.80	3.4	4.1	2.6	0.25
3	45	44.3	52.3	39.7	3.09	3.4	5.1	2.4	0.42
	90	41.1	50.7	36.7	2.38	3.3	4.8	2.6	0.29

Note: A_{mean}, A_{max}, A_{min}, and A_{std} are mean, maximum, minimum, and standard deviation values of cross-sectional area, respectively; t_{mean}, t_{max}, t_{min}, t_{std} are the mean, maximum, minimum, and standard deviation values of thickness, respectively.

The results of geometric measurements for both WAAM steel plates and HSS plates are presented in Table 6. For the sake of simplicity, detailed geometric information for only one HSS plate that matched each WAAM plate was provided. The thickness t was determined by averaging the thickness values obtained from a series of cross-sections taken along the specimen. The WAAM thickness t varied from 2.9 mm to 3.5 mm and the other detailed geometrical dimensions variation are shown in Table 6.

Table 6. Geometric measurement results of WAAM steel plates and high-strength steel plates

Specimens	d_{f} (mm)	t (mm)	d (mm)	b (mm)	e_1 (mm)	Matched specimens	t_{HSS} (mm)	d_{HSS} (mm)	b_{HSS} (mm)	$e_{1,\mathrm{HSS}}$ (mm)
HD3-18-30-27	16	3.4	18.4	30.1	26.3	HSS4-18-	4.0	17.8	30.6	26.1
VD3-18-30-27	16	3.3	17.8	30.2	24.1	30-27	4.0	17.6	31.1	28.7
HD3-18-40-27	16	3.3	18.4	39.6	25.5	HSS4-18-	4.0	17.7	41.0	25.2
VD3-18-40-27	16	3.3	18.0	39.5	26.2	40-27	4.0	17.7	41.3	26.5
HD3-18-60-27	16	3.5	17.9	60.6	26.5	HSS4-18-	4.0	17.9	60.9	27.4
VD3-18-60-27	16	3.1	17.8	60.5	26.3	60-27	4.0	17.9	61.2	27.6
HD3-18-70-27	16	3.3	18.0	69.7	26.6	HSS4-18-	4.0	17.9	72.0	27.6
VD3-18-70-27	16	3.2	17.8	69.6	25.7	70-27	4.0	18.0	71.9	27.1
HD3-18-70-36	16	3.4	18.2	69.6	35.1	HSS4-18-	4.0	17.9	71.3	36.9
VD3-18-70-36	16	3.3	17.8	70.2	36.5	70-36	4.0	17.7	71.5	36.8
HD3-18-70-54	16	3.4	17.9	69.6	54.2	HSS4-18-	4.0	17.7	71.7	54.6
VD3-18-70-54	16	3.1	17.8	69.4	53.3	70-54	4.0	17.9	71.2	54.8
HD3-18-100-63	16	3.3	17.8	99.7	62.6	HSS4-18-	3.9	17.8	100.9	62.9
VD3-18-100-63	16	3.4	17.8	99.4	62.3	100-63	4.0	18.0	101.7	63.3
HD3-18-100-66	16	3.2	17.4	99.6	64.0	HSS4-18-	4.0	17.8	101.8	66.3
VD3-18-100-66	16	3.1	17.8	99.4	64.5	100-66	4.0	18.0	101.1	66.7
HD3-18-110-72	16	3.2	17.4	110.0	72.8	HSS4-18-	4.0	17.8	112.2	72.3
VD3-18-110-72	16	3.2	17.8	110.0	70.5	110-72	4.0	17.6	111.2	72.1
HD3-22-50-33	20	3.4	21.6	50.0	32.4	HSS4-22-	4.0	20.0	51.5	32.4
VD3-22-50-33	20	3.1	21.6	50.7	32.8	50-33	4.0	23.0	51.0	33.5
HD3-22-70-33	20	3.3	21.6	69.4	33.0	HSS4-22-	4.0	23.0	71.3	33.7
VD3-22-70-33	20	3.1	21.4	69.5	33.3	70-33	4.0	23.3	71.2	33.5
HD3-22-90-53	20	3.5	21.9	88.1	53.0	HSS4-22-	4.0	22.4	91.3	53.5
VD3-22-90-53	20	3.4	21.4	88.5	51.9	90-53	4.0	22.9	91.9	52.9
HD3-22-100-77	20	3.4	21.8	99.6	74.8	HSS4-22-	4.0	22.4	101.2	77.6
VD3-22-100-77	20	3.4	21.6	99.5	76.2	100-77	4.0	21.9	101.5	77.4
HD3-22-130-77	20	3.2	21.4	130.2	76.2	HSS4-22-	4.0	23.3	130.7	77.8
VD3-22-130-77	20	3.2	21.6	129.9	77.6	130-77	4.0	22.8	131.9	77.6
HD3-26-80-65	24	3.5	26.0	79.5	67.8	HSS4-26-	3.9	25.8	80.0	65.7
VD3-26-80-65	24	3.2	26.2	79.8	64.9	80-65	4.0	25.8	82.4	65.2
HD3-26-110-65	24	3.4	26.0	109.9	64.8	HSS4-26-	4.0	26.3	112.3	64.8
VD3-26-110-65	24	3.4	26.0	109.8	65.6	110-65	4.0	26.3	112.1	64.6
HD3-26-140-96	24	3.2	26.0	140.1	95.8	HSS4-26-	4.0	26.4	142.0	95.7
VD3-26-140-96	24	3.6	25.8	140.1	97.9	140-96	4.0	26.6	141.5	96.2
HD3-26-150-104	24	3.4	26.0	147.1	102.7	HSS4-26-	4.0	26.3	151.7	103.7
VD3-26-150-104	24	3.2	26.0	148.0	103.8	150-104	4.0	26.5	151.8	104.6

3.3 Test Arrangements

All the coupon specimens and double-shear connection specimens were tested under tension until failure with a 250 kN Instron 8802 testing machine, as shown in Figure 4. The tests were displacement-controlled and conducted at room temperatures (20–25 °C). For the coupons, a constant stroke rate of 0.8 mm/min was used while for the lap shear specimens, the stroke rate was 1.0 mm/min.

Each double-shear connection was comprised of a WAAM plate and two matched high-strength steel plates, connected by a finger tightened high-strength bolt (Figure 4(a)). The contact between the bolt and steel plates occurred at the threaded portion of the bolt shank. An auxiliary plate was placed between the clamping ends of two high-strength steel plates to load the lap shear specimens under concentric load, as shown in Figure 4(a).

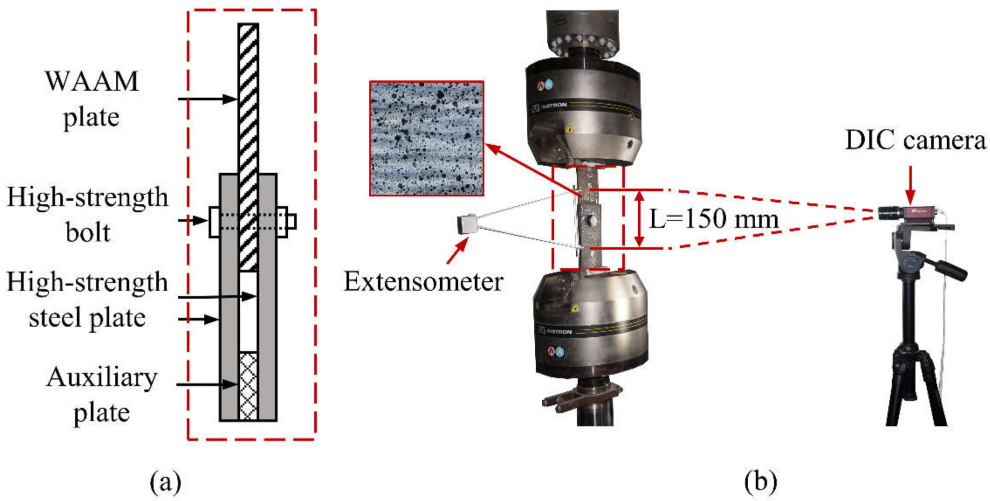

Figure 4. Schematic diagram of the experimental setup: (a) bolted connection; and (b) a typical test arrangement for lap shear connections

Digital Image Correlation (DIC) was adopted to measure the displacements over a length of 150 mm, as depicted in Figure 4(b). The test specimens were painted white and sprayed with a black random speckle pattern. A 5 Hz recording frequency was adopted. A conventional extensometer with a gauge length of 150 mm was used to measure the displacement between the two connection lap plates and provide reliable verification of the DIC system, as shown in Figure 5. The results obtained from the DIC system and the extensometer showed a negligible difference of less than 6%. As a result, data from the DIC system was used for subsequent data analysis.

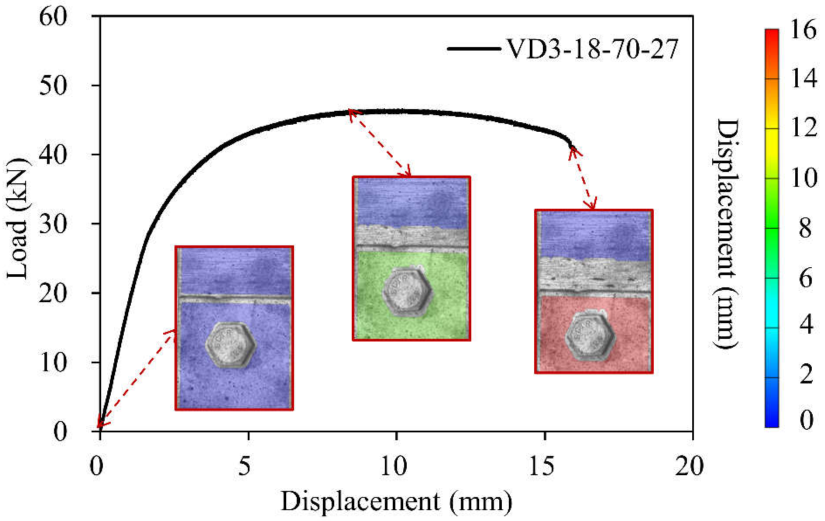

Figure 5. Displacements obtained by the DIC system

4. Test results

4.1 Material tests

The average material properties of the tested tensile coupons with print layer orientation θ of 0°, 45°, and 90°, including the Young's modulus E, yield strength f_y (defined as the 0.2% proof stress), ultimate tensile strength f_u, ultimate tensile strain ε_u, and fracture strain ε_f, are shown in Table 7.

Table 7. Average material properties for WAAM tensile coupons

Nominal thickness (mm)	Actual thickness (mm)	θ (°)	E (GPa)		f_{y} (MPa)		f_{u} (MPa)		ε_{u}		ε_{f}	
3	3.4	0	189	1.00	476	1.00	559	1.00	0.11	1.00	0.15	1.00
	3.6	45	214	1.13	412	0.87	518	0.93	0.07	0.64	0.08	0.53
	3.3	90	198	1.05	408	0.86	515	0.92	0.07	0.64	0.09	0.60

Results showed that the Young's modulus of the three groups of specimens was around 200 GPa, with values of 189 GPa, 214 GPa, and 198 GPa for specimens with 0°, 45°, and 90° angles, respectively. Other material properties for the specimens with a 90° angle were consistently lower compared to those with a 0° angle. The differences in yield strength, ultimate strength, ultimate tensile strain, and fracture strain reached up to 14%, 8%, 36%, and 40%, respectively. These findings demonstrated that the WAAM as-built specimens exhibited anisotropic material properties with strength differences (f_{y} and f_{u}) of up to 14% but a strain difference (ε_{y} and ε_{u}) of up to 40%.

The coupon test results showed that the material properties of WAAM steel could be dependent on the used feedstock and printing parameters. Differences of material properties have been found, compared to the results from Guo et al. [55, 56]. The yield strength and ultimate strength of tested coupons were approximately 10% higher than those in the literature. The ductility of the tested coupons was relatively low, with a minimum fracture strain of 0.08. The highest ductility was observed in the specimens with a θ angle of 0°, which showed the lowest ductility in the literature.

4.2 Double-shear connection tests

Figure 6 presents the five failure modes observed in the double-shear connection tests: (a) net section tension, (b) shear-out, (c) bearing, (d) end-splitting, and (e) block shear failure. Net section tension failure was mainly observed in the specimens with smaller plate widths, highlighted by the necking of the plates across the width and thickness (Figure 6(a)). Whilst, the shear-out specimens had relatively small end distances e_1 and the failure was characterized by the elongation of holes, longitudinal tears in the direction of the applied force, and piling of material, as shown in Figure 6(b).

Figure 6. Examples of failure modes: (a) net section tension, (b) shear-out, (c) bearing, (d) end-splitting, and (e) block shear

The bearing failure mode was observed in the specimens with larger widths and end distances.

Different from the shear-out failure mode, bearing failure was characterized by material piling up in front of the bolts, with no material extrusion from the plate end, as depicted in Figure 6(c). The end-splitting specimens exhibited fracture at the free end of the plate and significant rotation at the net cross-section, as depicted in Figure 6(d).

Only one specimen, VD3-22-70-33, exhibited fractures occurring at both the net tensile plane and the net shear plane, as illustrated in Figure 6(e), which was similar to the block shear failure in a single-bolted connection test by Guo et al. [56] but the fracture of VD3-22-70-33 originated at the free end of the plate due to the high transverse stress.

Figure 7 shows the load-displacement curves of test specimens grouped by conventional failure modes. The eleven load-displacement curves of net section tension specimens typically displayed a single ultimate point, with an abrupt declining branch afterwards. The net section tension specimens exhibited significantly smaller displacements at failure, as depicted in Figures 7(a) and (b).

Among the five shear-out specimens, most of them were specimens with a θ angle of 90° (VD specimens), as shown in Figure 7(c). The only block shear specimen was also a VD specimen (Figure 8). All five end-splitting specimens had a θ angle of 0° (HD specimens), as illustrated in Figure 7(d). The specimens with these three failure modes possessed very similar load-displacement curves.

Only the VD3-26-150-104 specimen exhibited an abnormally high ultimate load among the fourteen bearing specimens. The remaining specimens demonstrated comparable ultimate loads despite variations in their respective end distances, which ranged from 63 to 104, as shown in Figures 7(e) and (f).

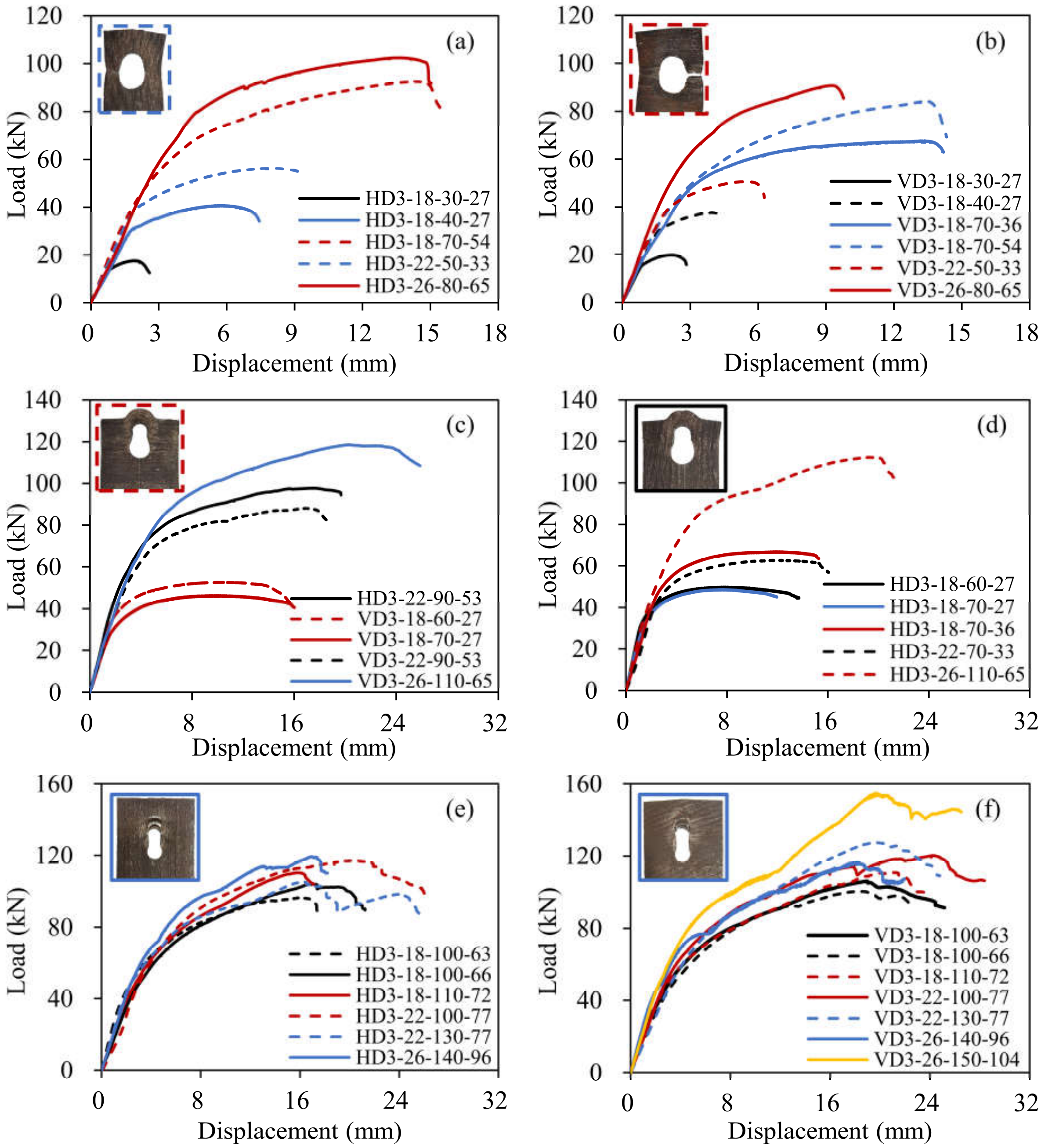

Figure 7. The load-displacement curve of WAAM lap shear specimens failed at different failure modes: (a) net section tension, θ = 0°; (b) net section tension, θ = 90°; (c) shear-out; (d) end-splitting; (e) bearing, θ = 0°; and (f) bearing, θ = 90°

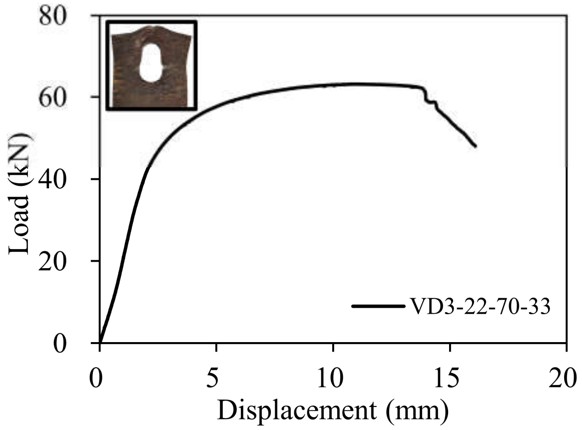

Figure 8. The load-displacement curve of VD3-22-70-33 failing by block shear

5. Experimental analysis and comparisons of design predictions

5.1 Material anisotropy

The study showed that the print layer orientation had a significant effect on the failure modes of the bolted connection specimens. Comparing pairs of specimens with the same nominal dimensions but different print layer orientations, it was observed that 28% of the pairs exhibited different failure modes. For each pair, the HD specimen tended to fail in end-splitting instead of expected shear-out, such as HD3-18-60-27/VD3-18-60-27 and HD3-18-70-27/VD3-18-70-27 in Figure 9.

The print layer orientation mainly affected the downstream materials of the above-mentioned specimens. During the testing process, the downstream plate material was compressed by the bolt, hence being subjected to shear stress τ and transverse tensile stress σ. The orientation of printed layers of the HD specimens in this region was perpendicular to the transverse tensile stress, rendering them more susceptible to end-splitting failure. On the contrary, the orientation of the printed layers of the VD specimens in this region was parallel to the direction of transverse tensile stress, providing sufficient resistance to prevent the formation of vertical cracks that initiated end-splitting failure.

Consequently, the orientation of print layers had an impact on the ultimate capacity of the specimens, shown by the normalised applied load $P/tf_{\mathrm{u,eff}}$ and displacement curves of the VD and HD specimens in Figure 9. Compared to the shear-out specimens, the end-splitting specimens generally exhibited smaller deformations and normalised loads. However, current standards do not explicitly distinguish between these two types of failures, which is highly unconservative for design.

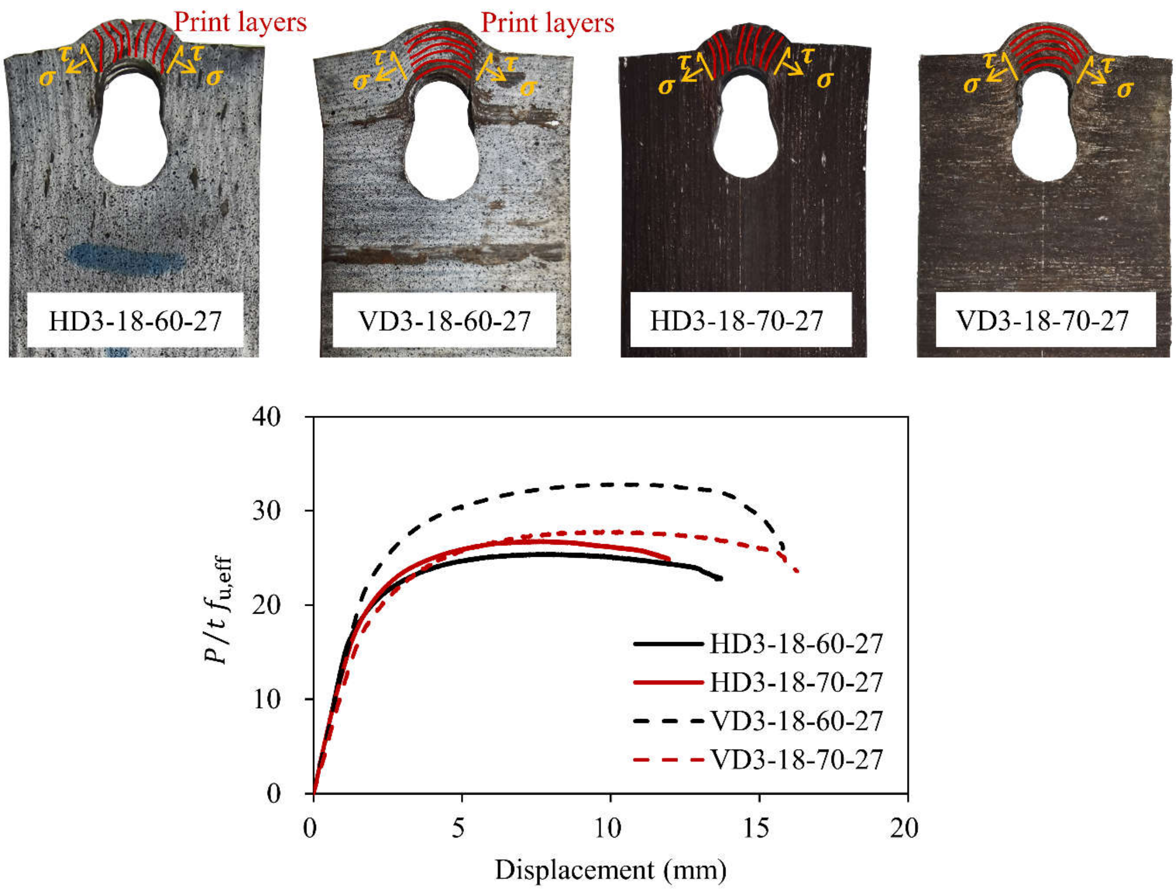

Figure 9. Examples and normalised load-displacement curves of the specimens with similar dimensions in different print layer orientations resulting in different failure modes

In addition, the differences in the ultimate capacity of the HD and VD specimens were sensitive to the print layer orientations. Figure 10 compares the normalised ultimate capacities of the HD and VD WAAM specimens, expressed as $P_{\mathrm{u},0°}/tf_{\mathrm{u,eff},0°}$ and $P_{\mathrm{u},90°}/tf_{\mathrm{u,eff},90°}$, respectively. The average ratio of $P_{\mathrm{u},90°}/tf_{\mathrm{u,eff},90°}$ and $P_{\mathrm{u},0°}/tf_{\mathrm{u,eff},0°}$ reached 1.14 with a coefficient of variation (COV) of 0.14, which showed that the normalized ultimate capacities of VD specimens were consistently higher than the HD specimens. The average difference of 14% exceeded the 8% variation in ultimate strength for tensile coupons with different print layer orientations.

In addition to the material anisotropy caused by print layer orientation, the significant different ultimate capacities of the VD and HD specimens in the same pair could be caused by potential process-induced defects in WAAM steel [10]. WAAM steel could have a higher probability for initial defects compared to traditional steel, resulting in a significant reduction in the ultimate capacity of WAAM bolted connection. As shown in Figure. 10, HD3-26-150-104/VD3-26-150-104 (point 1), HD3-22-130-77/VD3-22-130-7 (point 2), and HD3-18-60-27/VD3-18-60-27 (point 3), were beyond the range from 0.8 to 1.2. Despite the same failure mode, significant capacity disparities were shown up to 68% between specimen pairs represented by point 1 and point 2. HD3-26-150-104 and HD3-22-130-77 showed unexpectedly low ultimate capacities.

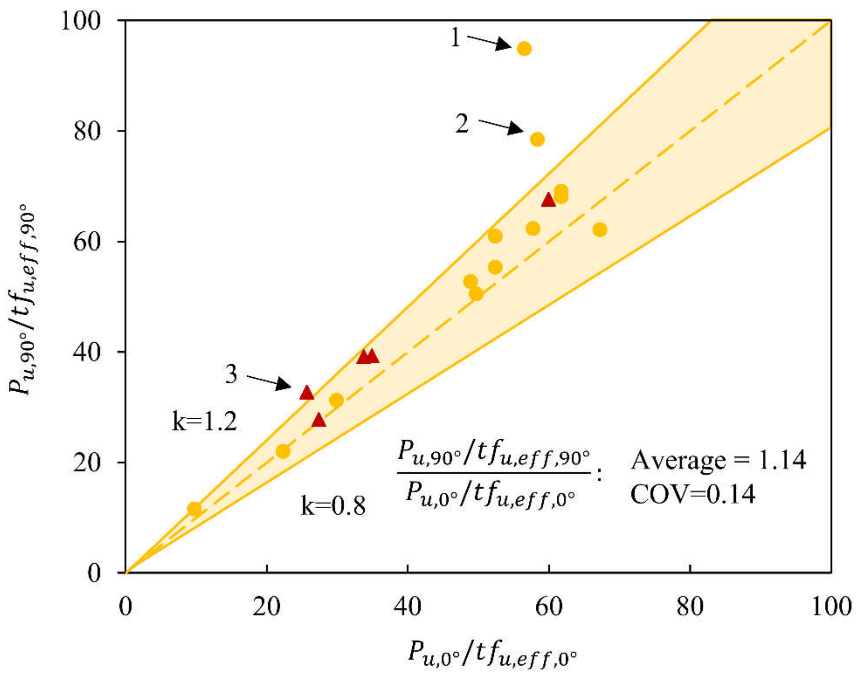

Figure 10. Comparison of different print layer orientations on ultimate capacities of lap shear connection tests (Triangles for specimen pairs with different failure modes, dots for specimens with the same failure mode)

5.2 Comparison of design predictions

5.2.1 Failure modes

The ultimate capacity predictions associated with different failure modes, such as net section tension, shear-out, and bearing failure, were calculated following the presented design provisions in section 2, based on the measured geometric parameters of the specimens. The failure mode corresponding to the minimum ultimate capacity was considered as the predicted failure mode. The comparisons between the predictions and the experimental results in terms of failure mode and ultimate capacities are presented in Table 8.

The six standards showed similar overall prediction accuracies for failure modes. The accuracy percentages varied from 64% to 69%, with a mean value of 67%, as shown in Figure 11. Although EN 1993-1-3 [50] and EN 1993-1-8 [51] exhibited the highest accuracy percentage of 69%, the two codes remained unsatisfying predictions. Particularly, the current standards did not consider the end-splitting failure mode, which led to incorrect failure mode predictions for the end-splitting specimens. For instance, specimen HD3-18-60-27 failed in end-splitting but all standards had the same prediction of shear-out failure. Therefore, incorporating the prediction of end-splitting failure capacities of 3D-printed bolted connections in the existing design codes should be considered.

Table 8. Summary of experimental results and comparisons with design codes

Specimen	Test		AISI S100		AISC 360		EN 1993-1-3		EN 1993-1-8		AS/NZS 4600		AS4100		Eq.4	Eq.5	Eq.6	Eq.7
	FM	P_u (kN)	FM	$\frac{P_u}{P_{AISI}}$	FM	$\frac{P_u}{P_{AISC}}$	FM	$\frac{P_u}{P_{EN3}}$	FM	$\frac{P_u}{P_{EN8}}$	FM	$\frac{P_u}{P_{AS/NZS}}$	FM	$\frac{P_u}{P_{AS}}$	$\frac{P_u}{P_{so,1}}$	$\frac{P_u}{P_{so,2}}$	$\frac{P_u}{P_{so,3}}$	$\frac{P_u}{P_b}$
HD3-18-30-27	NS	18.26	NS	0.87	NS	0.83	NS	0.83	NS	0.83	NS	0.87	NS	0.98				
HD3-18-40-27	NS	41.24	SO	1.14	NS	1.05	NS	1.05	SO	1.12	NS	1.12	SO	1.37				
HD3-18-60-27	ES	50.41	SO	1.22	SO	0.98	SO	1.16	SO	1.20	SO	0.97	SO	1.46	0.97	0.92	1.16	
HD3-18-70-27	ES	49.83	SO	1.30	SO	1.04	SO	1.24	SO	1.29	SO	1.03	SO	1.56	1.03	0.97	1.24	
HD3-18-70-36	ES	67.04	SO	1.12	SO	0.90	SO	1.19	SO	1.26	SO	0.99	SO	1.34	0.95	0.92	1.21	
HD3-18-70-54	NS	92.16	NS	1.02	B	1.02	B	1.22	B	1.13	NS	1.02	NS	1.11				
HD3-18-100-63	B	96.41	B	0.82	B	1.09	B	1.31	B	1.21	SO	0.84	B	1.02				0.94
HD3-18-100-66	B	103.74	B	0.90	B	1.20	B	1.44	B	1.34	B	0.90	B	1.13				1.03
HD3-18-110-72	B	110.46	B	0.97	B	1.29	B	1.54	B	1.43	B	0.97	B	1.21				1.10
HD3-22-50-33	NS	56.31	SO	1.15	NS	1.05	SO	1.11	SO	1.11	NS	1.12	SO	1.38				
HD3-22-70-33	ES	62.55	SO	1.27	SO	1.01	SO	1.23	SO	1.23	SO	1.02	SO	1.52	1.02	0.96	1.18	
HD3-22-90-53	SO	97.62	SO	0.98	B	0.83	SO	1.12	SO	1.14	SO	0.94	SO	1.18	0.87	0.86	1.10	
HD3-22-100-77	B	116.97	NS	0.86	B	1.03	B	1.23	B	1.14	NS	0.86	SO	0.97				0.88
HD3-22-130-77	B	104.96	SO	0.74	B	0.97	B	1.17	B	1.08	SO	0.77	B	0.91				0.83
HD3-26-80-65	NS	102.38	NS	1.05	NS	0.98	NS	0.98	NS	0.98	NS	1.05	NS	1.15				
HD3-26-110-65	ES	112.42	SO	0.96	B	0.83	SO	1.11	SO	1.11	SO	0.93	SO	1.16	0.86	0.85	1.07	
HD3-26-140-96	B	119.34	B	0.70	B	0.93	B	1.12	B	1.04	B	0.70	B	0.88				0.80
HD3-26-150-104	B	108.87	B	0.59	B	0.78	B	0.94	B	0.87	B	0.59	B	0.74				0.67
VD3-18-30-27	NS	19.79	NS	0.98	NS	0.93	NS	0.93	NS	0.93	NS	0.98	NS	1.10				
VD3-18-40-27	NS	37.70	NS	1.09	NS	1.02	NS	1.02	NS	1.02	NS	1.09	SO	1.28				
VD3-18-60-27	SO	52.65	SO	1.57	SO	1.25	SO	1.49	SO	1.39	SO	1.25	SO	1.88	1.25	1.18	1.48	

VD3-18-70-27	SO	46.38	SO	1.38	SO	1.10	SO	1.30	SO	1.20	SO	1.08	SO	1.65	1.09	1.02	1.28	
VD3-18-70-36	NS	67.59	SO	1.19	SO	0.95	SO	1.29	SO	1.20	SO	1.08	SO	1.42				
VD3-18-70-54	NS	84.23	NS	1.11	B	1.10	B	1.32	SO	1.10	NS	1.11	NS	1.20				
VD3-18-100-63	B	106.01	B	0.96	B	1.27	B	1.52	B	1.27	SO	0.98	B	1.19				1.09
VD3-18-100-66	B	100.53	B	0.98	B	1.30	B	1.56	B	1.30	B	0.98	B	1.22				1.11
VD3-18-110-72	B	110.84	B	1.07	B	1.42	B	1.70	B	1.42	B	1.07	B	1.33				1.22
VD3-22-50-33	NS	50.61	SO	1.18	NS	1.07	SO	1.14	NS	1.07	NS	1.14	SO	1.42				
VD3-22-70-33	BS	63.18	SO	1.44	SO	1.16	SO	1.41	SO	1.26	SO	1.18	SO	1.73				
VD3-22-90-53	SO	88.19	SO	1.02	B	0.84	SO	1.17	SO	1.04	SO	0.97	SO	1.23	0.90	0.89	1.11	
VD3-22-100-77	B	120.23	NS	0.96	B	1.15	B	1.38	B	1.15	NS	0.96	B	1.08				0.99
VD3-22-130-77	B	127.38	B	0.98	B	1.31	B	1.57	B	1.31	SO	1.01	B	1.23				1.12
VD3-26-80-65	NS	90.62	NS	1.11	NS	1.03	NS	1.03	NS	1.03	NS	1.11	NS	1.21				
VD3-26-110-65	SO	118.66	SO	1.07	B	0.94	SO	1.24	SO	1.12	SO	1.03	SO	1.29	0.95	0.95	1.19	
VD3-26-140-96	B	116.41	B	0.65	B	0.86	B	1.04	B	0.86	B	0.65	B	0.81				0.74
VD3-26-150-104	B	154.89	B	0.99	B	1.32	B	1.58	B	1.32	B	0.99	B	1.24				1.13
FMPA			0.64		0.67		0.69		0.69		0.64		0.67					
Mean				1.04		1.05		1.24		1.15		0.98		1.24	0.99	0.95	1.20	0.98
COV				0.20		0.15		0.17		0.13		0.14		0.20	0.11	0.09	0.09	0.17

Note: FM = failure mode; NS: net section tension; SO: shear-out; ES: end-splitting; B: bearing; BS: block shear failure; FMPA: failure mode prediction accuracy and COV: coefficient of variation.

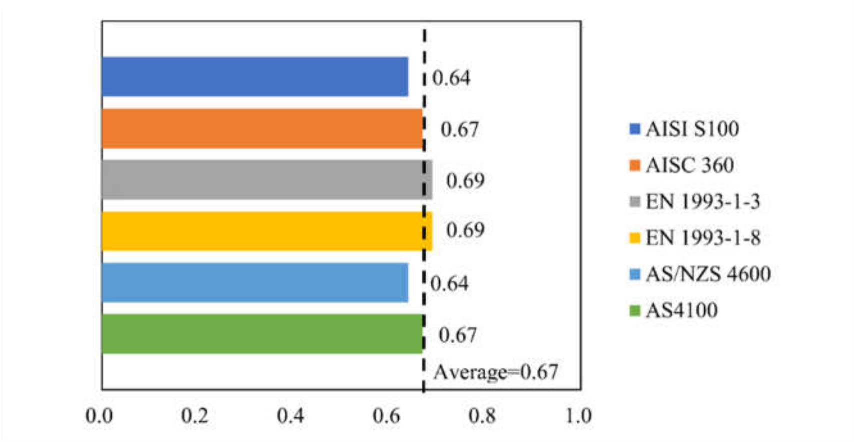

Figure 11. Prediction accuracies of failure modes in six standards

5.2.2 Ultimate capacities

Table 8 presents comparisons of ultimate capacities between test results ($P_{\mathrm{u,exp}}$) and predictions ($P_{\mathrm{u,pre}}$). Overall, the average test-to-predicted capacity ratios ($P_{\mathrm{u,exp}}/P_{\mathrm{u,pre}}$) fluctuated between 0.98 and 1.24 for the design standards. The ultimate capacities could be better predicted by the design codes than failure modes. This could be attributed to the fact that the ultimate capacities for end-splitting failure and shear-out failure were relatively similar, despite the incorrect prediction of failure mode. The AS/NZS 4600 [45] showed the best prediction with an average $P_{\mathrm{u,exp}}/P_{\mathrm{u,pre}}$ ratio of 0.98 and a COV of 0.14. However, AS 4100 [46] exhibited the most conservative predictions, with a 19% in $P_{\mathrm{u,exp}}/P_{\mathrm{u,pre}}$ ratio and a COV of 0.20.

To evaluate the suitability of current design methods for WAAM steel bolted connections for each failure mode, further analyses were conducted in the subsequent sections. Figure 12 presents the average $P_{\mathrm{u,exp}}/P_{\mathrm{u,pre}}$ ratio and the COV for different failure modes predicted by various design codes of practice. For the net section tension failure mode, except for AS 4100

[46], the predictions of ultimate capacities were generally accurate and stable. AS 4100 [46] tended to predict net section tension specimens (such as HD3-18-40-27 and VD3-22-50-33) with a shear-out failure mode. A smaller shear coefficient and shear plane length were used, resulting in a lower capacity prediction for shear-out failure than that for net section tension failure. AISC 360 [48] showed the best predictions with an average $P_{\mathrm{u,exp}}/P_{\mathrm{u,pre}}$ of 1.01 and a COV of less than 0.07.

As discussed in Section 5.1, the capacity and failure mode predictions of WAAM bolted connections could be influenced by the initial defects caused by the undulating surfaces of the as-built WAAM specimens, which might result in an unconservative design. For instance, most design codes presented an overestimation of the ultimate capacity for the specimen HD3-18-40-27 which might be due to the defects produced during the manufacturing process. Therefore, more stringent safety or material factors should be adopted in the future codes and guidelines for additively manufactured bolted connections.

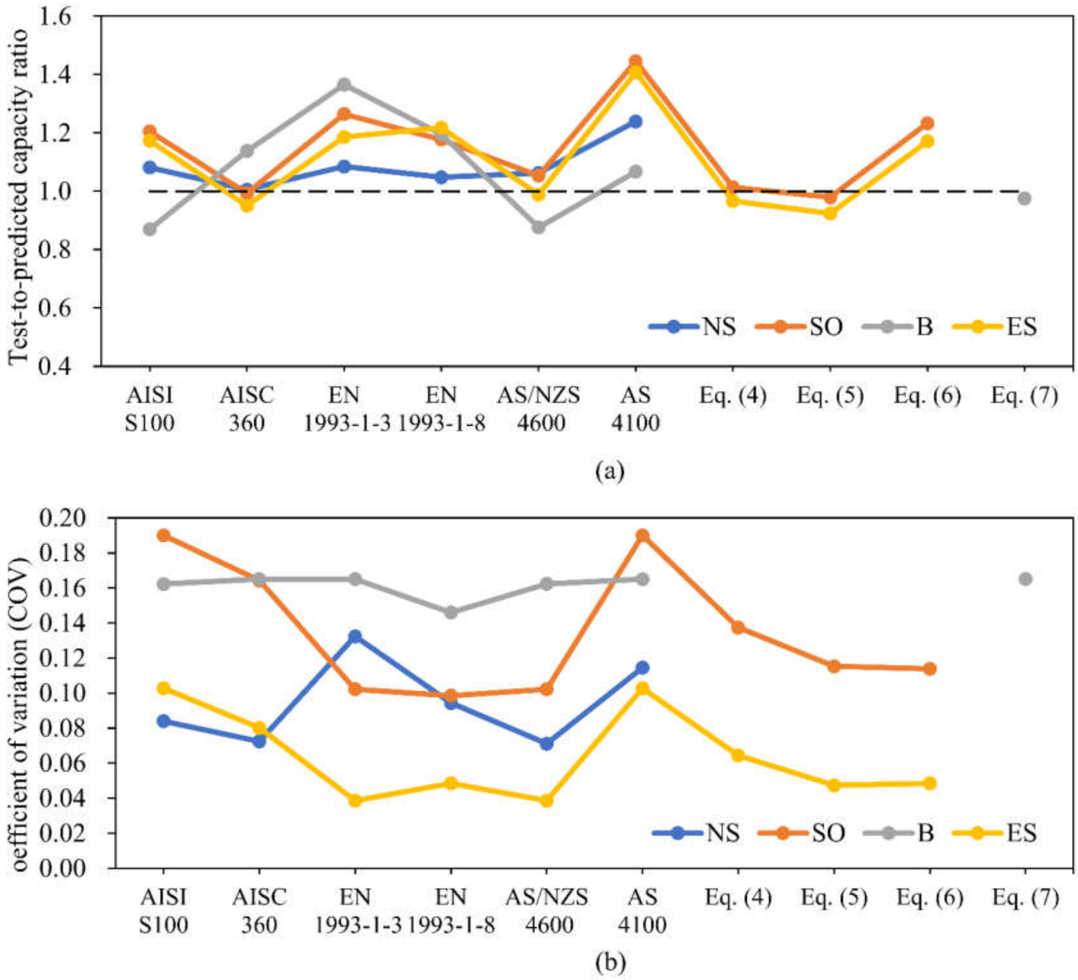

Figure 12. Evaluation of different codes towards different failure modes

For shear-out specimens, the $P_{\mathrm{u,exp}}/P_{\mathrm{u,pre}}$ ratios and COVs varied considerably among different design standards, mainly because of the different shear plane lengths and coefficients embedded in the equations. AISC 360 [48] had the best performance, with a slightly overestimation of 1% and a relatively lower COV of 0.16. Among the proposed equations in the existing literature, Eq. (4) [43] had the best prediction for shear-out failure, with an underestimation of 1% and a COV of 0.11.

The average ratios of test-to-predicted capacity for bearing failure specimens ranged from 0.87 to 1.37. Eq. (7) [34] provided the most accurate predictions with an average ratio of 0.98.

Among all the standards, AS 4100 [46] provided the most accurate predictions with an average ratio of 1.07. However, all design codes exhibited a COV greater than 0.15, indicating lower prediction stability compared to net section tension failure, as shown in Figure 12(b).

The end-splitting failure mode was widely recognized as the transitional mode between net section tension failure and shear-out failure [53, 54]. End-splitting failures of the specimens were often predicted to be a shear-out failure, as shown in Table 8, as the end-splitting failure has not been incorporated in the design standards. Though with the wrong failure mode prediction, AS/NZS 4600 [45] provided the most accurate predictions for ultimate capacity, as shown in Figure 12. It had an overestimation of only 1% and a COV of 0.04.

Lyu et al. [54] took the end-splitting failure in Eq. (6), where e_1/e_2 = 0.5 as the boundary of shear-out and end-splitting failure. With e_1/e_2 over 0.5, end-splitting failure predictions could be made by adding a strength reduction factor of 0.9, based on the proposed shear-out failure predictions. However, all the test specimens had a ratio e_1/e_2 over 0.5 but only five end-splitting specimens were observed. This reduced the validity of Eq. (6) [54] for WAAM steel bolted connections.

It is worth noting that the relatively accurate predictions for the ultimate capacity were compromised by incorrect failure mode predictions. The available specifications for conventionally steel structures were not sufficient to design WAAM manufactured bolted connections. Future research is needed to improve the existing design equations to achieve satisfying predictions of failure modes and ultimate capacities.

6. Conclusions

In this paper, a total of 24 coupon specimens and 36 double-shear connection specimens were tested, with different print layer orientations and varying geometrical dimensions. The study analysed and discussed the influence of print layer orientations on WAAM material properties and the effect of WAAM material properties on bolted connections. The current design codes for traditional steel structures were evaluated against the test results. Based on the results, the following conclusions were drawn:

1) Apart from the Young's modulus, the material properties of as-built WAAM coupons, including yield strength, ultimate strength, ultimate tensile strain, and fracture strain, presented some extent of anisotropy. The four properties of specimens with a θ= 0° were consistently higher than specimens with a θ = 90°, as the difference of ultimate tensile strength and ultimate strain of specimens with different print layer orientations reached up to 8% and 40%, respectively.

2) Five distinct failure modes, including net section tension, shear-out, bearing, end-splitting, and block shear failure were observed for the WAAM bolted shear connection specimens. The orientation of the print layers (θ = 0° and 90°) affected both the failure modes and ultimate capacity. 28% specimens with the same nominal dimensions but different print layer orientations showed different failure modes but a 14% difference in the ultimate capacity predictions.

3) The design standards were not sufficient to provide accurate predictions for the failure modes of WAAM lap shear specimens, as shown by the ratio of prediction ranged from 64% to 69%. This could be attributed to the anisotropic material properties of the WAAM steel plates and the neglection of end-splitting failure modes in current design standards.

4) Among the existing design standards, the best prediction for the ultimate capacity of WAAM lap shear specimens was from AS/NZS 4600, with a test-to-predicted capacity ratio of 0.98 and a coefficient of variation (COV) of 0.14. For the failure modes of net section tension, shear-out, and bearing failure, the best predictions were provided by AISC 360 [48], AISC 360 [48], and AS 4100 [46], respectively.

5) Among the equations presented in literature, the ultimate capacities of specimens failed in bearing and shear-out modes could be accurately predicted by equations proposed by Teh and Uz [34, 43] with test-to-prediction ratios of 0.98 and 0.99, respectively. However, further research is required regarding the design approach for end-splitting failure in WAAM steel.

6) The structural performance of WAAM steel bolted connections could be influenced by the initial defects. It could result in an unconservative design, which means more stringent resistance factors should be adopted in the future design guidelines for 3D-printed bolted connections.

Acknowledgement

The authors would like to thank the financial supports from the National Natural Science Foundation of China (NSFC) (Grant Number: 52208215), the Natural Science Foundation of Zhejiang Province (Grant Number: LQ22E080008) and the Centre for Balance Architecture of Zhejiang University. The author would also like to thank the code for WAAM geometry analysis provided by the Steel Structures Group of Imperial College London.

Reference

[1] L. Gardner, Metal additive manufacturing in structural engineering – review, advances, opportunities and outlook, Structures, 47 (2023) 2178-2193.

[2] J. Ye, P. Kyvelou, F. Gilardi, H. Lu, M. Gilbert and L. Gardner, An end-to-end framework for the additive manufacture of optimized tubular structures, IEEE Access, 9 (2021) 165476-165489.

[3] L. Gardner, P. Kyvelou, G. Herbert and C. Buchanan, Testing and initial verification of the world's first metal 3D printed bridge, Journal of Constructional Steel Research, 172 (2020) 106233.

[4] C. Buchanan and L. Gardner, Metal 3D printing in construction: a review of methods, research, applications, opportunities and challenges, Engineering Structures, 180 (2019) 332-348.

[5] T. Duda and L. V. Raghavan, 3D metal printing technology: the need to re-invent design practice, Ai & Society, 33 (2018) 241-252.

[6] C. R. Cunningham, J. M. Flynn, A. Shokrani, V. Dhokia and S. T. Newman, Invited review article: strategies and processes for high quality wire arc additive manufacturing, Additive Manufacturing, 22 (2018) 672-686.

[7] S. I. Evans, J. Wang, J. Qin, Y. He, P. Shepherd and J. Ding, A review of WAAM for steel construction – manufacturing, material and geometric properties, design, and future directions, Structures, 44 (2022) 1506-1522.

[8] A. Kanyilmaz, A. G. Demir, M. Chierici, F. Berto, L. Gardner, S. Y. Kandukuri, P. Kassabian, T. Kinoshita, A. Laurenti, I. Paoletti, A. du Plessis and N. Razavi, Role of metal

3D printing to increase quality and resource-efficiency in the construction sector, Additive Manufacturing, 50 (2022) 102541.

[9] T. D. Ngo, A. Kashani, G. Imbalzano, K. T. Q. Nguyen and D. Hui, Additive manufacturing (3D printing): a review of materials, methods, applications and challenges, Composites Part B: Engineering, 143 (2018) 172-196.

[10] B. Wu, Z. Pan, D. Ding, D. Cuiuri, H. Li, J. Xu and J. Norrish, A review of the wire arc additive manufacturing of metals: properties, defects and quality improvement, Journal of Manufacturing Processes, 35 (2018) 127-139.

[11] D. Ding, Z. Pan, D. Cuiuri and H. Li, Wire-feed additive manufacturing of metal components: technologies, developments and future interests, The International Journal of Advanced Manufacturing Technology, 81 (2015) 465-481.

[12] V. Laghi, M. Palermo, G. Gasparini, V. A. Girelli and T. Trombetti, On the influence of the geometrical irregularities in the mechanical response of wire-and-arc additively manufactured planar elements, Journal of Constructional Steel Research, 178 (2021) 106490.

[13] L. Tonelli, R. Sola, V. Laghi, M. Palermo, T. Trombetti and L. Ceschini, Influence of interlayer forced air cooling on microstructure and mechanical properties of wire arc additively manufactured 304L austenitic stainless steel, steel research international, 92 (2021) 2100175.

[14] N. Hadjipantelis, B. Weber, C. Buchanan and L. Gardner, Description of anisotropic material response of wire and arc additively manufactured thin-walled stainless steel elements, Thin-Walled Structures, 171 (2022) 108634.

[15] T. J. Dodwell, L. R. Fleming, C. Buchanan, P. Kyvelou, G. Detommaso, P. D. Gosling, R. Scheichl, W. S. Kendall, L. Gardner, M. A. Girolami and C. J. Oates, A data-centric approach to generative modelling for 3D-printed steel, Proc Math Phys Eng Sci, 477 (2021) 20210444.

[16] J. Müller, J. Hensel and K. Dilger, Mechanical properties of wire and arc additively manufactured high-strength steel structures, Welding in the World, 66 (2021) 395-407.

[17] J. Ge, J. Lin, Y. Long, Q. Liu, L. Zhang, W. Chen and Y. Lei, Microstructural evolution and mechanical characterization of wire arc additively manufactured 2Cr13 thin-wall part, Journal of Materials Research and Technology, 13 (2021) 1767-1778.

[18] V. Laghi, L. Tonelli, M. Palermo, M. Bruggi, R. Sola, L. Ceschini and T. Trombetti, Experimentally-validated orthotropic elastic model for wire-and-arc additively manufactured stainless steel, Additive Manufacturing, 42 (2021) 101999.

[19] P. Kyvelou, H. Slack, D. Daskalaki Mountanou, M. A. Wadee, T. B. Britton, C. Buchanan and L. Gardner, Mechanical and microstructural testing of wire and arc additively manufactured sheet material, Materials & Design, 192 (2020) 108675.

[20] C. Huang, P. Kyvelou, R. Zhang, T. Ben Britton and L. Gardner, Mechanical testing and microstructural analysis of wire arc additively manufactured steels, Materials & Design, 216 (2022) 110544.

[21] C. Guo, M. Liu, R. Hu, T. Yang, B. Wei, F. Chen and L. Zhang, High-strength wire + arc additive manufactured steel, International Journal of Materials Research, 111 (2020) 325-331.

[22] L. Sun, F. Jiang, R. Huang, D. Yuan, C. Guo and J. Wang, Anisotropic mechanical properties and deformation behavior of low-carbon high-strength steel component fabricated by wire and arc additive manufacturing, Materials Science and Engineering: A, 787 (2020) 139514.

[23] Z. Lin, C. Goulas, W. Ya and M. J. M. Hermans, Microstructure and mechanical properties of medium carbon steel deposits obtained via wire and arc additive manufacturing using metal-cored wire, Metals, 9 (2019) 673.

[24] P. Kyvelou, H. Slack, C. Buchanan, M. A. Wadee and L. Gardner, Material testing and analysis of WAAM stainless steel, 4 (2021) 1702-1709.

[25] C. Huang, P. Kyvelou and L. Gardner, Stress-strain curves for wire arc additively manufactured steels, Engineering Structures, 279 (2023) 115628.

[26] V. Laghi, L. Arrè, L. Tonelli, G. Di Egidio, L. Ceschini, I. Monzón, A. Laguía, J. A. Dieste and M. Palermo, Mechanical and microstructural features of wire-and-arc additively manufactured carbon steel thick plates, The International Journal of Advanced Manufacturing Technology, 127 (2023) 1391-1405.

[27] C. Huang, X. Meng and L. Gardner, Cross-sectional behaviour of wire arc additively manufactured tubular beams, Engineering Structures, 272 (2022) 114922.

[28] P. Kyvelou, C. Huang, L. Gardner and C. Buchanan, Structural testing and design of wire arc additively manufactured square hollow sections, 147 (2021) 04021218.

[29] V. Laghi, M. Palermo, G. Gasparini, V. A. Girelli and T. Trombetti, Experimental results for structural design of wire-and-arc additive manufactured stainless steel members, Journal of Constructional Steel Research, 167 (2020) 105858.

[30] C. Huang, X. Meng, C. Buchanan and L. Gardner, Flexural buckling of wire arc additively manufactured tubular columns, Journal of Structural Engineering, 148 (2022) 04022139.

[31] R. Scharf-Wildenhain, A. Haelsig, J. Hensel, K. Wandtke, D. Schroepfer and T. Kannengiesser, Heat control and design-related effects on the properties and welding stresses in WAAM components of high-strength structural steels, Welding in the World, 67 (2022) 955-965.

[32] T. S. Kim, H. Kuwamura and T. J. Cho, A parametric study on ultimate strength of single shear bolted connections with curling, Thin-Walled Structures, 46 (2008) 38-53.

[33] A. G. Kamtekar, On the bearing strength of bolts in clearance holes, Journal of Constructional Steel Research, 79 (2012) 48-55.

[34] L. H. Teh and M. E. Uz, Combined bearing and shear-out capacity of structural steel bolted connections, Journal of Structural Engineering, 142 (2016) 04016098.

[35] C. Ding, S. Torabian and B. W. Schafer, Strength of bolted lap joints in steel sheets with small end distance, Journal of Structural Engineering, 146 (2020) 04020270.

[36] M. D. Elliott, L. H. Teh and A. Ahmed, Behaviour and strength of bolted connections failing in shear, Journal of Constructional Steel Research, 153 (2019) 320-329.

[37] P. Može, Bearing strength at bolt holes in connections with large end distance and bolt pitch, Journal of Constructional Steel Research, 147 (2018) 132-144.

[38]G. Winter, Tests on bolted connections in light gage steel, Journal of the Structural Division, 82 (1956) 920-1-920-25.

[39] H. J. Kim and J. A. Yura, The effect of ultimate-to-yield ratio on the bearing strength of bolted connections, Journal of Constructional Steel Research, 49 (1999) 255-269.

[40] L. H. Teh and B. P. Gilbert, Net section tension capacity of bolted connections in cold-reduced steel sheets, 138 (2012) 337-344.

[41] L. H. Teh and D. D. A. Clements, Block shear capacity of bolted connections in cold-reduced steel sheets, Journal of Structural Engineering, 138 (2012) 459-467.

[42] D. D. A. Clements and L. H. Teh, Active shear planes of bolted connections failing in block shear, Journal of Structural Engineering, 139 (2013) 320-327.

[43]L. H. Teh and M. E. Uz, Ultimate shear-out capacities of structural-steel bolted connections, Journal of Structural Engineering, 141 (2015) 04014152.

[44] H. Xing, L. H. Teh, Z. Jiang and A. Ahmed, Shear-out capacity of bolted connections in cold-reduced steel sheets, Journal of Structural Engineering, 146 (2020) 04020018.

[45] AS/NZS 4600, Cold-formed steel structures, AS/NZS 4600:2018, Sydney, Australian/New Zealand Standard, 2018.

[46] AS 4100, Steel structures, AS 4100:2020, Australia, Standards Association of Australia, 2020.

[47] AISI S100, North American specification for the design of cold-formed steel structural members, AISI S100–16w/S1-18, Washington DC, American Iron and Steel Institue, 2016.

[48] AISC 360, Specification for structural steel buildings, ANSI/AISC 360-22, Chicago, American Institute of Steel Construction, 2022.

[49] Eurocode 3: design of steel structures – part 1-1: general rules and rules for builidng, prEN 1993-1-1, Brussels, European Committee for Standardisation, 2020.

[50] Eurocode 3 - design of steel structures - part 1-3: general rules - supplementary rules for cold-formed members and sheeting, prEN 1993-1-3, Brussels, European Committee for Standardisation, 2022.

[51] Eurocode 3: design of steel structures – part 1-8: design of joints, prEN 1993-1-8, Brussels, European Committee for Standardisation, 2021.

[52] H. Teh Lip and E. Uz Mehmet, Ultimate tilt-bearing capacity of bolted connections in cold-reduced steel sheets, Journal of Structural Engineering, 143 (2017) 04016206.

[53] Y. B. Wang, Y. F. Lyu, G. Q. Li and J. Y. R. Liew, Behavior of single bolt bearing on high strength steel plate, Journal of Constructional Steel Research, 137 (2017) 19-30.

[54] Y. F. Lyu, Y. B. Wang, G. Q. Li and J. Jiang, Numerical analysis on the ultimate bearing resistance of single-bolt connection with high strength steels, Journal of Constructional Steel Research, 153 (2019) 118-129.

[55] X. Guo, P. Kyvelou, J. Ye, L. H. Teh and L. Gardner, Experimental investigation of wire arc additively manufactured steel single-lap shear bolted connections, Thin-Walled Structures, 181 (2022) 110029.

[56] X. Guo, P. Kyvelou, J. Ye, L. H. Teh and L. Gardner, Experimental study of DED-arc additively manufactured steel double-lap shear bolted connections, Engineering Structures, 281 (2023) 115736.